Renewable Energy 179 (2021) 1217–1232

Contents lists available at ScienceDirect

Renewable Energy

journal homepage: www.elsevier.com/locate/renene

High performance solar receiver–reactor for hydrogen generation

A. Lidor [a, b, *], T. Fend [b], M. Roeb [b], C. Sattler [b]

[a] Department of Mechanical and Process Engineering, ETH Zürich, 8092, Zürich, Switzerland
[b] Institute of Solar Research, German Aerospace Center (DLR), 51143, Köln, Germany

ARTICLE INFO

Article history:
Received 7 March 2021
Received in revised form
1 July 2021
Accepted 19 July 2021
Available online 29 July 2021

Keywords:
Solar energy
Thermochemical cycles
Hydrogen generation
Solar fuels

ABSTRACT

This paper reports on the numerical analysis of a volumetric solar receiver-reactor for hydrogen production, using the 2-step reduction–oxidation cycle. A detailed parametric sweep covering hundreds of various parameter combinations is performed for a large solar reactor, using a transient physical model. We generate performance maps which are currently cost prohibitive via experimental or high–fidelity simulation studies. The following performance metrics are evaluated: solar to fuel efficiency, hydrogen yield, conversion extent and specific hydrogen yield. We show that the relations between the different performance metrics are complex, leading to different optimal points depending on the metric pursued. The daily hydrogen yield for a single reactor varied between 0.89 kg for an absorber thickness of 30 mm, and up to 1.04 kg for a 60 mm thick receiver, with solar to fuel efficiency values of 3.84% and 3.81% respectively. For a case with 45 mm thick receiver, an intermediate hydrogen yield of 0.94 kg is calculated, while exhibiting the highest efficiency (4.05%). The efficiency can be further increased to 5.86% by using a simple heat recovery system, and reach an upper limit of 21.16% with a more sophisticated heat recovery method.

1. Introduction

Hydrogen is a critically important energy carrier used for many applications in the chemical industry, transportation, and energy sectors. Therefore, the sustainable production of hydrogen is an important research topic in recent years, driven by environmental, economic and engineering considerations. While there are several different approaches to the production of hydrogen that are being pursued today, the use of solar–driven thermochemical process remains a promising candidate to replace classical hydrogen production methods [1–3]. The solar–driven thermochemical process for hydrogen production is a two–step reduction–oxidation cycle, used for splitting water into hydrogen and oxygen. The high temperature heat required for the endothermic reduction reaction is achieved by using concentrated sunlight, where a metal oxide is reduced and oxygen is released. Following this step, an exothermic oxidation reaction occurs when water reacts with the reduced oxide, whereupon the water molecules split into hydrogen and oxygen, and the oxygen is absorbed back in the oxide. While several families of reduction–oxidation (redox) materials have been developed and tested over the years, non-stoichiometric cerium oxide remains one of the most promising candidates for the water splitting reaction [4–7]. The reduction reaction is formulated as

$$CeO_{2-\delta_{ox}} \rightarrow CeO_{2-\delta_{red}} + \frac{\delta_{red} - \delta_{ox}}{2} O_2, \quad (1)$$

and the oxidation step is given by

$$CeO_{2-\delta_{red}} + (\delta_{red} - \delta_{ox}) H_2O \rightarrow CeO_2 - \delta_{ox} + (\delta_{red} - \delta_{ox}) H_2. \quad (2)$$

The redox cycle is presented in Fig. 1. To date, volumetric solar reactors with absorbers made of monolithic or porous structures have shown the most promising results for this technology. Various designs and configurations of such reactors have been demonstrated in different scales, under real sunlight conditions [8–12] or in solar simulators [13,14]. Other concepts for solar reactors have been pursued as well, including isothermal ceria reactors [15,16], counter-rotating reactors [17], particle reactors [18], and membrane reactors [5,19], as well as fluidized bed reactors with $NiFe_2O_4$ and CeO_2 particles [20,21].

While there are many different solar thermal and chemical applications, using both line and point focus systems, the current

* Corresponding author. Department of Mechanical and Process Engineering, ETH Zürich, 8092, Zürich, Switzerland.
E-mail address: alidor@ethz.ch (A. Lidor).

https://doi.org/10.1016/j.renene.2021.07.089

Nomenclature

Roman symbols

A	Area, m^2
A_0	Pore specific surface area, $m^2\,m^{-3}$
C	Concentration, $kg\,m^{-3}$
c_p	Specific heat capacity, $J\,kg^{-1}\,K^{-1}$
D	Diameter, m
d_m	Mean pore diameter, m
F	Forchheimer (inertial) coefficient, m^{-1}
h	Heat transfer coefficient, $W\,m^{-2}\,K^{-1}$
h_{sf}	Interfacial heat transfer coefficient, $W\,m^{-2}\,K^{-1}$
K	Permeability, m^2
K_c	Equilibrium constant
k_e	Effective thermal conductivity, $W\,m^{-1}\,K^{-1}$
M	Molar mass, $kg\,kmol^{-1}$
m	Mass, kg
$\dot{m}$	Mass flow, $kg\,h^{-1}$
$\dot{m}''$	Oxygen release rate, $kg\,m^{-2}\,s^{-1}$
n	Total amount, mol
$\dot{n}$	Molar flow rate, $mol\,s^{-1}$
Nu	Nusselt number
p	Pressure, Pa
$\dot{q}$	Volumetric heat generation, $W\,m^{-3}$
Q	Thermal energy, kJ
q	Solar power, kW
$\dot{Q}$	Heat transfer rate, W
R	Universal gas constant, $J\,kg^{-1}\,K^{-1}$
r	Reaction rate, $mol\,s^{-1}$
Re	Reynolds number
T	Temperature, K
$\mathbf{u}$	Fluid velocity vector, $m\,s^{-1}$
X	Conversion extent

Greek symbols

β	Extinction coefficient, m^{-1}
δ	Nonstoichiometry extent
ΔG	Gibbs free energy, $kJ\,kmol^{-1}\,K^{-1}$
Δt	Time step, s
Δx	Cell size, m
ϵ	Porosity
ε	Emissivity
η	Solar to fuel efficiency
μ	Viscosity, Pa s
φ	Volume fraction in foam
ρ	Density, $kg\,m^{-3}$
τ	Transmissivity

Subscripts

abs	Absorber
amb	Ambient
cd	Cooldown
CeO_2	Ceria
chem	Chemical
f	Fluid
H_2	Hydrogen
H_2O	Steam
HR	Heat recovery
in	Inlet
N_2	Nitrogen
O_2	Oxygen
ox	Oxidation
red	Reduction
r	Radiation
s	Solid
win	Window

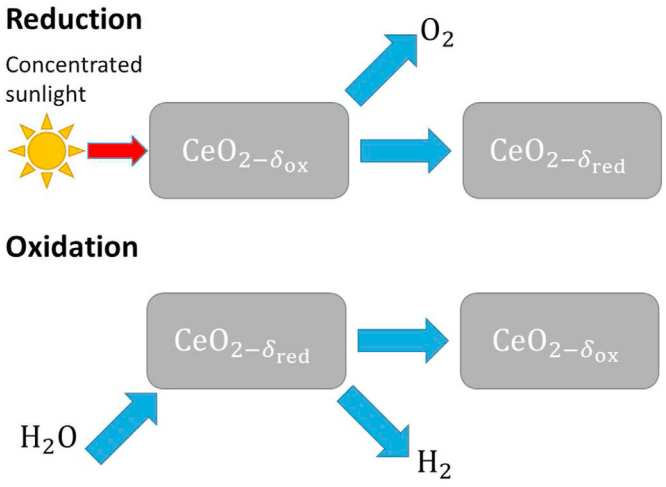

Fig. 1. Solar–driven 2-step reduction–oxidation cycle for water splitting.

work deals with reactors operating with point focus systems only. This is due to the high temperature required for the redox cycle, which can only be achieved using point focus systems [22,23]. Another important aspect of solar thermochemical processes is the redox material. Different materials have been investigated in recent years, both volatile and nonvolatile [1,24]. While volatile materials theoretically present higher oxygen exchange capabilities, the recombination effects associated with them present a challenge which has not been countered successfully to date [1,25]. On the other hand, non-stoichiometric ceria has been considered as a promising candidate early on in the research of solar thermochemistry applications [26], though different studies in recent years focused on the thermodynamic and kinetic properties [27,28]. A recent review paper about ceria redox cycles provides a detailed overview of the current status of the experimental work in this field [4].

Extensive modelling efforts of different solar reactors have been performed over the years, to support the expensive and complex development of high temperature solar reactor systems. A solar–driven thermochemical cycle using solid–solid heat recuperation system has been proposed and modelled by Lapp et al. [29,30]. The concept is based on counter–rotating cylinders that allows for continuous fuel production and heat recovery. The outer cylinder is made of a porous reactive oxide material, while the inner cylinder is made of an inert material, responsible on recovering the heat from the oxide material. A flow of inert gas is used for sweeping the oxygen released from the oxide layer. A transient three–dimensional heat transfer model has been developed for this concept. Heat recovery effectiveness of up to 95% and solar–to–fuel efficiency of up to 5% were predicted for a steady-state reactor operation. Another reactor concept, consisting of a cavity reactor

with an array of annular reactive elements, has been analysed using a three–dimensional CFD model [31]. This reactor concept is based on using porous ceria monoliths with integrated gas inlet and outlet channels, allowing for an isothermal operation and both continuous or batch fuel production. Two configurations for the reactor were evaluated, with the predicted oxygen production rates of 40–60 μmol s^{-1} and average redox material temperatures of 1660–1680 K. The ZnO cycle has been studied as well, due to its potential for high energy conversion efficiency [32]. The ZnO dissociation process has been modelled in a three–dimensional CFD analysis, where the model was validated against experimental results for a 10 kW and was then used to evaluate the performance of a larger 1 MW reactor. It was shown that the solar–to-chemical conversion efficiency can be increased over 50% for the large 1 MW reactor when operating at temperatures above 2000 K. In a recent work, a packed–bed solar reactor, designed for the reduction of iron–manganese particles, has been evaluated by Wang et al. [33]. A transient CFD model, including detailed heat and mass transfer, has been developed and validated experimentally. Following the model development and validation, it was used in conjunction with experimental results to calculate the thermochemical performance of the reactor. The peak instantaneous solar–to–chemical energy conversion efficiency was found to be 9.3%, with an average reactor cavity temperature of almost 1200 K. An extensive review of solar thermochemical reactors have been performed by Wheeler et al. [34], in which a large number of numerical modelling efforts are described and discussed. Their work includes various categorization criteria of such modelling works, i.e. discrete vs. continuum scales, experimental properties vs. ab initio calculations, reactor configurations, and more. In their work, several main challenges for the modelling of solar thermochemical reaction systems have been identified. They have also proposed some directions and guidelines for the research in this field. A general thermodynamic analysis for countercurrent reactor systems, based on second law of thermodynamics analysis and mas balance limitations, has been developed and applied to various membrane reactors and the ceria redox cycle [35]. It has been shown that countercurrent reactors for thermochemical fuel production outperform cocurrent reactors on the order of 1–2 times. A more detailed general thermodynamic analysis, focused on the nonstoichiometric redox cycle, has been performed [36]. In this work, several state–of–the–art and hypothetical materials have been analysed in a counterflow reactor system. Global efficiency maps are presented for the redox materials, revealing that ceria–based materials are superior to perovskites in most cases. It is also shown that competing factors in the system, strongly coupled to the material properties, are limiting the operational conditions of such systems. Especially when aiming for conditions in or close to the optimal operational conditions, the design requires materials which are currently unavailable. For the optimal hypothetical materials at optimal conditions, efficiencies of up to 32.7% are predicted, with some higher values for several specific cases with a large temperature swing or high heat recovery effectiveness.

The objective of this paper is to thoroughly investigate the operation of a large scale solar reactor, and to analyse potential gains from various possible improvements, both in operation and design. In our past study [37] we focused on the reduction step of the solar reactor, characterizing its performance and investigating the effects of several parameters on the possible extent of reduction, with the maximum potential hydrogen yield of 5.25 g/cycle. This was achieved by using MONROE (Model for N_2–operated receiver–reactor), a custom finite volume method code developed at DLR. In this work, we present several various additions to the MONROE code, as well as a more detailed analysis. The complete reduction–oxidation cycle is investigated and we develop new concepts for implementation in the solar reactor: heat recovery during both reduction and oxidation steps and variable sweep gas flow rate. We also perform an analysis over a whole day, studying the cycling behaviour of the reactor. These concepts can be adapted to volumetric solar reactors and increase the solar to fuel efficiency and hydrogen yield, exceeding 4% and reaching about 130 g/cycle, respectively. In addition, several unique challenges are identified for the ASTOR[1] reactor, which can be improved in the next generation reactor, as well as by other research groups worldwide. The results presented in this work are based on physical modelling of the transient behaviour of the system, offering physical insights in order to realistically evaluate performance gains, serving as a cost-effective alternative for testing a wide parameter range using extensive experimental or high–fidelity simulation studies.

2. Numerical model

The analysis of the ASTOR reactor is performed using the MONROE code, which is detailed in a previous paper [37]. The solar reactor consists of a directly irradiated receiver, made of a porous ceria–coated zirconia. Unlike vacuum operated reactors, this reactor achieves the required low oxygen partial pressure by a continuous flow of sweep gas (nitrogen) through the reactor cavity during the reduction step. The front of the reactor is sealed by a quartz window, through which concentrated sunlight enters the cavity and irradiates the receiver. Upon completion of the reduction step, the solar energy input is ceased completely (or at least decreased) and the reactor cools down. Once the desired oxidation temperature is achieved, the flow of nitrogen is replaced by a flow of steam into the reactor. The steam flows through the porous receiver, being split into hydrogen while the ceria is being re-oxidised. A sketch of the ASTOR reactor is presented in Fig. 2 and the complete system flowchart is given in Fig. 3.

Since the MONROE model equations have been provided in detail in a previous paper [37], this work includes only the main equations, as well as several specific improvements and additions made to the original model.

2.1. Model equations

The model solves a combined heat and mass transfer problem in the reactor. The main domain of the model is the porous receiver, comprised of a solid and fluid phases. In addition, the cavity in front of the reactor and at the receiver back are included in the model as fluid domains, while the reactor walls and insulation are included as solid domains. The properties of the receiver material are presented in Table 1. Applicable correlations from Ref. [38] were used in the cases where the effects of different porous material properties were studied (in lieu of the specific values for the ASTOR current receiver material).

The conservation of energy in the solid phase is given by

$$\frac{\partial}{\partial t}\left[(1-\epsilon)\rho_s c_{p_s}\langle T_s\rangle\right] = \nabla\cdot(k_e\nabla\langle T_s\rangle) + \dot{q}_r + \dot{q}_{chem} + h_{sf}A_0\left(\langle T_f\rangle - \langle T_s\rangle\right), \quad (3)$$

while the conservation of energy in the fluid phase is

[1] The project name which stands for “automation of solar thermochemical cycles to reduce hydrogen production costs”.

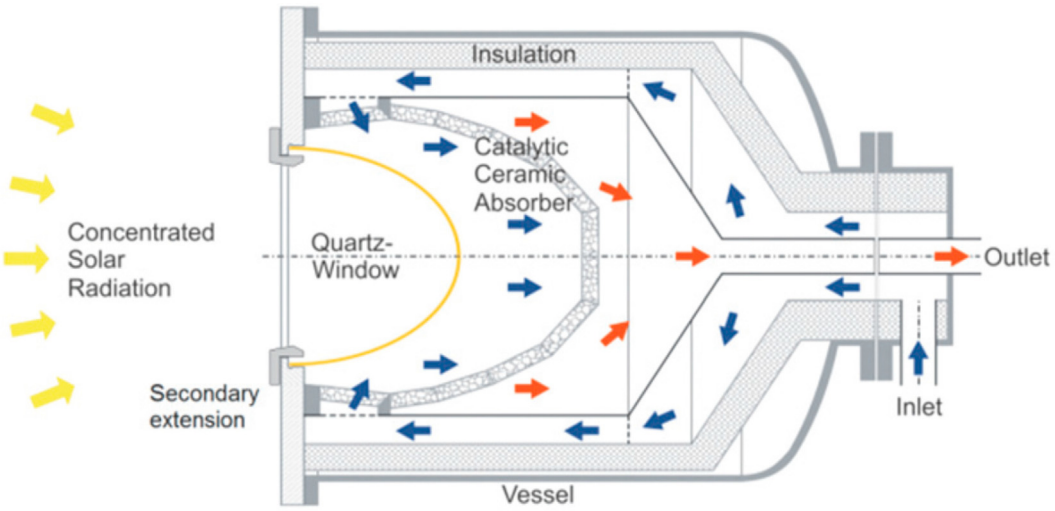

Fig. 2. The ASTOR reactor: a large scale volumetric directly irradiated porous receiver–reactor [37]. The blow arrows are for the inlet stream, red arrows are for the outlet stream after passing through the receiver.

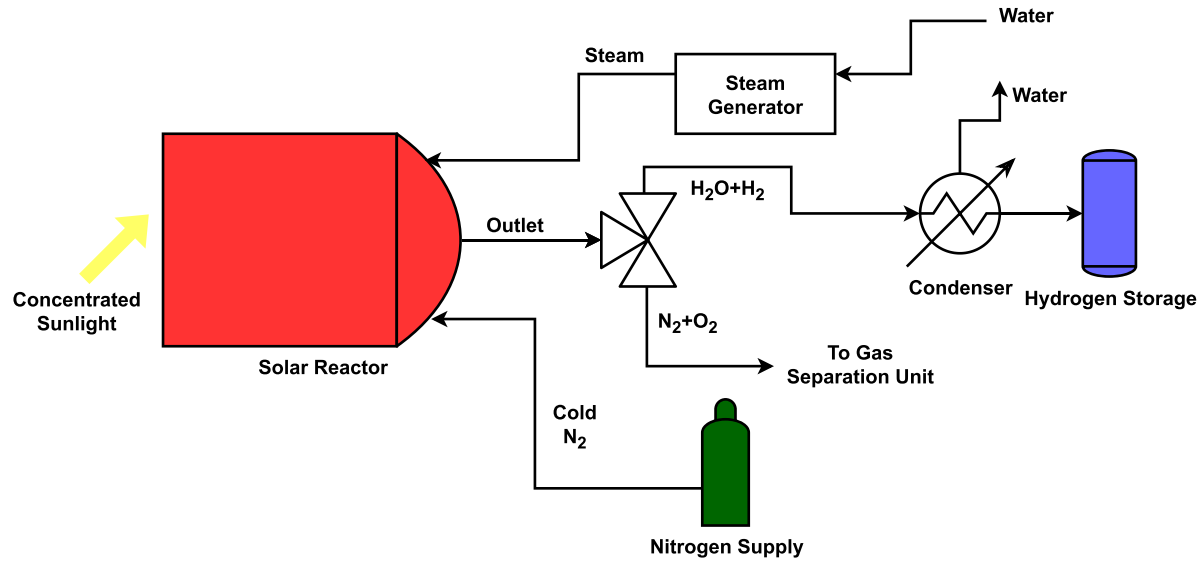

Fig. 3. System flowchart for normal operation (without heat recovery).

$$\frac{\partial}{\partial t}\left(\epsilon\rho_f c_{p_f}\langle T_f\rangle\right)+\nabla\cdot\left(\epsilon\mathbf{u}\rho_f c_{p_f}\langle T_f\rangle\right) = \nabla\cdot\left(k_f\nabla\langle T_f\rangle\right) + h_{sf}A_0\left(\langle T_s\rangle-\langle T_f\rangle\right) \tag{4}$$

The mixture is assumed to behave as an ideal gas, following the Dalton law, and all the thermophysical properties of the different fluids (N_2, O_2, H_2O, H_2) are taken from the NIST Chemistry WebBook [40] as temperature–dependent correlations. The flow regime is assumed to be laminar, since the problem deals with low Reynolds numbers (Re < 150) within the inertial flow regime [46]. For the flow analysis, the Darcy–Forchheimer law is used:

$$\nabla\langle p\rangle_f = -\frac{\mu_f}{K}\langle\mathbf{u}\rangle - F\rho_f\langle\mathbf{u}\rangle\langle\mathbf{u}\rangle \tag{5}$$

The conservation of species is solved by the convection–diffusion equation for the oxygen in the fluid phase:

$$\frac{\partial}{\partial t}\left(\epsilon C_{O_2}\right)+\frac{\partial}{\partial x}\left(uC_{O_2}\right)=\frac{\partial}{\partial x}\left(D_{O_2,\mathrm{eff}}\frac{\partial C_{O_2}}{\partial x}\right)+\dot{m}''A_0. \tag{6}$$

For the radiation analysis within the porous receiver, the Rosseland diffusion approximation (RDA) for optically thick medium is applied, while the volumetric absorption of the solar radiation follows a Beer–Lambert law. The radiation exchange within the reactor is included in the model, as well as a spillage factor and window transmissivity, as detailed in Table 2.

Model additions The major addition to the MONROE model is the inclusion of the oxidation step, as well as a wide range of calculations for cycle performance. In principle, the thermal behaviour of the reactor is identical in all stages of operation, except the chemical terms, which consists of endothermic reaction in the reduction step, inert operation during the cooldown phase, and an exothermic oxidation step. Since the flow rates in the oxidation step are very small, the method of a quasi-steady state approximation is used, in a similar manner to Venstrom [50], Warren [51]

Table 1
Physical properties and correlations of the solid phase [37].

Parameter	Correlation	Units	Ref
CeO_2 properties			
Density	$\rho_{CeO_2} = 7215$	kg m^{-3}	[39]
Molar mass	$M_{CeO_2} = 172.115$	kg kmol^{-1}	[40]
Specific heat capacity	$c_{p,CeO_2} = \frac{67.95 - 9.9 \times 10^5 T^{-2} + 0.0125T}{M_{CeO_2}}$	J kg^{-1} K^{-1}	[41]
ZrO_2 properties			
Density	$\rho_{ZrO_2} = 5680$	kg m^{-3}	[39]
Molar mass	$M_{ZrO_2} = 123.223$	kg kmol^{-1}	[40]
Specific heat capacity	$c_{p,ZrO_2} = 3.03193 \times 10^{-7}T^3 - 9.41346 \times 10^{-4}T^2 + 1.02303T + 229.958$	J kg^{-1} K^{-1}	[42]
Foam properties			
Ceria fraction in foam	$\varphi_{CeO_2} = 0.25$		[37]
Mean pore diameter	$d_m = b_0\epsilon + b_1$	m	[38]
Specific surface area	$A_0 = -a_0\epsilon^2 + a_1\epsilon + a_2$	m^2 m^{-3}	[38]
Permeability	$K = 3.60528 \times 10^{-7}$	m^2	[43]
Forchheimer coefficient	$F = 3.6992 \times 10^{-2}$	m^{-1}	[43]
Thermal conductivity	$k_s = 0.5615$	W m^{-1} K^{-1}	[44]
Nonstoichiometry extent	$\delta = 0.35\frac{8700 p_{O_2}^{0.217} exp(-195.6/RT)}{1 + 8700 p_{O_2}^{0.217} exp(-195.6/RT)}$		[45]
Enthalpy of reduction	$\Delta h_{red} = \left(478 - 1158\delta + 1790\delta^2 + 23368\delta^3 - 64929\delta^4\right) \times 10^3$	J mol^{-1}	[27]

and Brendelberger [52]. Using this assumption, the oxidation is assumed to be fast at every point in the reactor at each time step. By using the law of mass action

$$K_c = \frac{\left(\frac{p_{H_2}}{p_0}\right)\left(\frac{p_{O_2}}{p_0}\right)^{1/2}}{\left(\frac{p_{H_2O}}{p_0}\right)}, \quad (7)$$

the partial pressures can be correlated to the equilibrium constant which is given by

$$K_c = \exp\left(-\frac{\Delta G}{RT}\right) \quad (8)$$

The Gibbs free energy ΔG is calculated from the same correlations used in calculating the other fluid properties [40]. The total released oxygen is calculated from

$$n_{O_2} = \int r_{O_2,red} dt \quad (9)$$

and the hydrogen generated is

$$n_{H_2} = \int r_{H_2,ox} dt. \quad (10)$$

The steam conversion extent is given by

$$X_{H_2O} = -r_{H_2}\frac{\epsilon V_{abs}}{\dot{n}_{H_2O}}. \quad (11)$$

The chemical energy released during oxidation is neglected, making our oxidation analysis more conservative, since the released heat would have helped in slowing the inevitable cooling of the reactor during the oxidation step.

Table 2
Optical parameters for the model.

Parameter	Value	Units	Ref
Receiver porosity	$\epsilon = 0.7$		[37]
Receiver emissivity	$\varepsilon_{abs} = 0.7$		[47]
Extinction coefficient	$\beta = 420.5$	m^{-1}	[48, 38]
Window transmissivity	$\tau_{win} = 0.95$		[49]
Spillage factor	$\eta_{spil} = 0.9$		[49]

2.1.1. Boundary and initial conditions

The boundary and initial conditions are specified in Table 3 for a standard base case. Some of the parameters are varied as the performance of the system is investigated.

2.2. Numerical method

In principle, MONROE uses a finite volume method in a 1D space and a uniform mesh. The solid cells are piecewise-linear while the fluid cells use the exponential scheme. The Gauss–Seidel method was used to solve the system of equations, and the standard convergence checks and error estimations described in our previous work were repeated whenever a major change of parameters occurred. A standard time step $\Delta t = 1$ s and element size $\Delta x = 6 \times 10^{-4}$ m were used, except in some specific runs where higher accuracy was required. The full details of the numerical methods employed in the model and its validation are provided in the previous paper [37].

3. Results

The extended model was used in the analysis of the ASTOR reactor, with the actual system parameters, as well as extensive study of the effects of various parameters on its performance. We begin with a detailed analysis of the standard case, and continue to present the results of various advanced concepts that we identify as relevant for pushing this technology towards economic viability.

3.1. Standard case

We have analysed the reactor performance identically to the first characterization runs of the ASTOR reactor (with input parameter values as per Table 3). The switching conditions between the cycles were based on the average receiver temperatures. The reduction end temperature $T_{red,\ end}$ was set to 1100 °C, while oxidation start temperature was set to $T_{ox,\ start} = 850$ °C. The end of oxidation and starting of the next cycle was set to $T_{ox,\ end} = 650$ °C. Fig. 4 shows the mean temperature of the receiver and of the sweep gas flowing through the reactor as a function of time. We can see that when comparing mean temperatures, there is no noticeable difference between the solid and fluid temperatures. A clear explanation for the low mean temperature is achieved when examining the temperature profile across the receiver in different

Table 3
Input parameters for the model including boundary and initial conditions.

Parameter	Symbol	Value	Ref
Absorber thickness	L	0.06 m	a
Absorber diameter	D_{abs}	0.662 m	a
Absorber surface area	A_{abs}	1.36 m^2	a
Total ceria mass	m_{Ce}	53.26 kg	a
Initial solid temperature	$T_{s,0}$	25 °C	b
Inlet N_2 temperature	T_{in,N_2}	25 °C	b
Inlet steam temperature	T_{in,H_2O}	150 °C	b
Heat transfer coefficient (ambient–window)	h_{amb}	5 W m^{-2} K^{-1}	[53]
Nusselt number (N_2 at frontal cavity–window)	Nu_{win}	5	[54]
Nusselt number (N_2 at frontal cavity–absorber)	Nu_{abs}	5	[54]
N_2 mass flow	$\dot{m}_{N_2}$	20 kg h^{-1}	b
Steam mass flow	$\dot{m}_{H_2O}$	5 kg h^{-1}	b
Solar power	q	150 kW	b

[a]Input data taken from the ASTOR reactor dimensions.
[b]Value used in the ASTOR experiments.

stages: reduction end, oxidation start (end of cooldown phase), and oxidation end. The results are presented in Fig. 5a, showing a steep temperature gradient across the receiver at the end of the reduction step, as was previously noticed [37]. However, having the analysis results for the complete cycle, it is now obvious that due to this large gradient, the temperature profile drastically shifts during the cooldown phase. During this shift the receiver temperature drops significantly at the receiver front, while the temperature at the back of the reactor actually still increases initially. The temperature decrease at the front of the receiver is mostly due to re-radiation losses, but is also due to the cold fluid (N_2 or H_2O, depending on the step) which enters the front of the receiver. In the meantime, the conduction and convection across the porous receiver contributes to the temperature increase at the back of the receiver. We also note that being the first cycle of the day, the reduction step starts from ambient temperature, leading not only to a longer step but also to a larger temperature gradient across the receiver. If we compare this to the temperature profile of the second cycle, following the end of the first cycle, we can see that the reduction time decreases from 31 min to 8 min (Fig. 5b). Additionally we can see that the temperature at the back of the receiver remains almost constant, due to the different temperature profile at the start of the cycle.

The hydrogen production capabilities and reactor performance for both cases are presented in Table 4 (volumes are at STP conditions). It is noted that even though the reactor starts at a higher temperature in the second cycle compared to the first cycle, the overall cycle duration is only shorter by about 4 min. While reduction during the second cycle is of course much shorter, the cooldown and oxidation steps are about 1.5 times longer compared to the first cycle. This is attributed to the re-radiation from the front being the major cooling mechanism. Since the re-radiation term is dependent on the receiver temperature, but also on its optical properties, the first few millimetres are the most dominant in determining the re-radiation heat transfer rate. As we have shown in our previous study, the 60 mm receiver is an optical thick medium, with a very low volumetric absorption. Hence, the temperature at the front of the receiver is the dominant factor in determining the cooldown duration, and in this case the first cycle temperature profile is more favourable for a shorter cooldown (the same applies to the oxidation step). Another noteworthy result is that contrary to the expectations, the performance of the second cycle is significantly lower than that of the first cycle, in terms of hydrogen production and steam conversion extent. This is explained by looking at the temperature profile at the end of the reduction. While the temperature profile gradient during the first cycle is steeper than that of the second cycle, the underlying physics are more complicated than one might assume. The extent of reduction (non-stoichiometry extent) is a function of both oxygen partial pressure and temperature (see Table 1). However, even at lower oxygen partial pressures, a high enough temperature is required for a meaningful reduction, as presented in Fig. 6. During the first cycle, the front of the receiver achieves such a temperature and is significantly reduced (while the back remains oxidised). However, during the second cycle the limited reduction in the front is not compensated by the slightly higher temperature at the back of the receiver. Another possible effect could be that due to the large thickness of the receiver, some of the generated hydrogen at the front actually reduces the ceria at the back, thus destroying some of the generated hydrogen within the porous receiver. The maximum possible H_2 in Table 4 refers to the amount of hydrogen that can be generated if complete re-oxidation of the ceria is achieved, under the level of non-stoichiometry extent that was reached at the end of the reduction step. It is clear from this that the current design, coupled with the existing operation mode, suffers from both poor reduction and oxidation steps that prevent the reactor producing even the expected hydrogen yield for the relatively low reduction extent.

In the next parts we investigate an array of parameters, both operational and geometrical, in order to study their effects on the performance and propose improvements for the solar reactor.

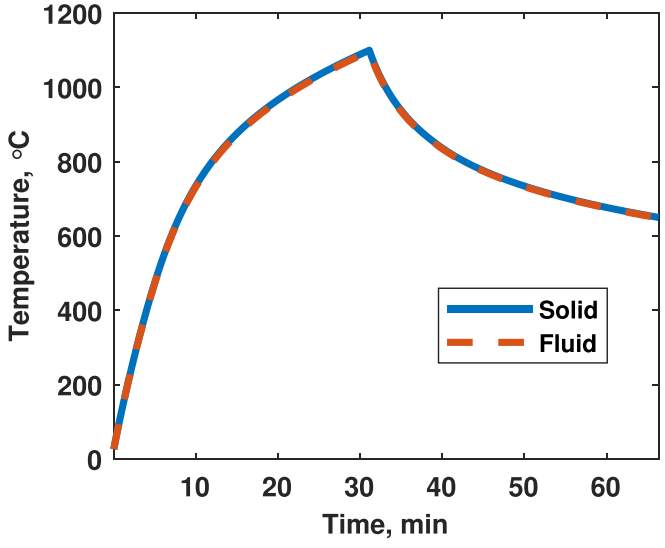

Fig. 4. Mean solid and fluid temperature as a function of time over one cycle.

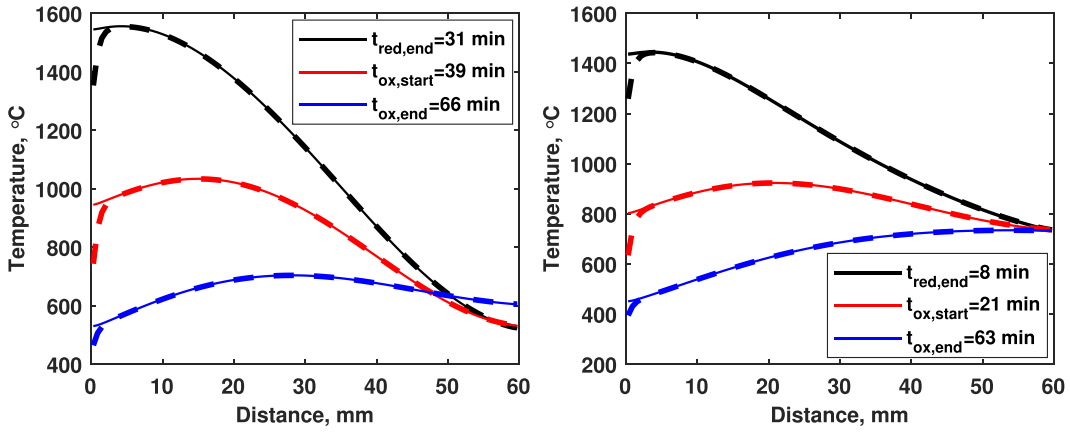

(a) First cycle (b) Second cycle

Fig. 5. Solid and fluid temperature across the receiver at different steps for: (a) the first cycle (starting from cold reactor); and (b) second cycle (starting from a hot reactor).

Table 4
Results of the normal case for the first and second cycles.

Parameter	Cycle 1	Cycle 2
Reduction duration	31.2 min	8.4 min
Cooldown duration	8.1 min	12.2 min
Oxidation duration	27.2 min	42.1 min
Average reduction temperature	1100 °C	1100 °C
Maximum reduction temperature	1556 °C	1445 °C
Total released O_2	52.00 L	22.76 L
Generated H_2	5.81 L	0.19 L
Maximum possible H_2	131.88 L	57.74 L
Maximum steam conversion extent	0.0873%	0.0109%

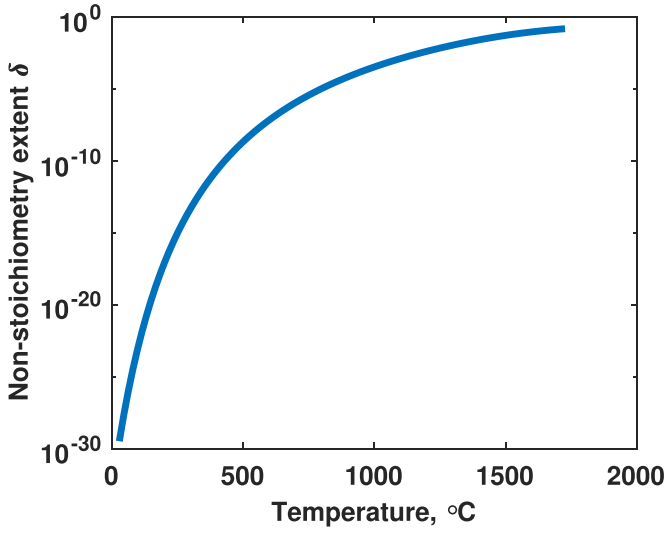

Fig. 6. Ceria non-stoichiometry extent vs. temperature for constant oxygen partial pressure $p_{O_2} = 10^{-5}$ bar.

3.2. Advanced reactor concepts

We have seen that the standard case has a limited potential for hydrogen production. Moreover, under the current operation conditions, the reactor is operating at a much lower effectiveness than this limit. Taking into account the results from our previous study, there are several improvements that are beneficial for the reactor in terms of the reduction step effectiveness. While some of these improvements for the reduction step might have negative effects on the overall cycle performance, others are clearly beneficial for the overall performance, without any competing effects between the reduction and oxidation steps. Most important among them is the porous receiver composition - the ASTOR receiver is currently made of ceria–coated zirconia, made of 25% mass-based ceria. This porous material has been manufactured a few years ago, and with the rapid improvement in foam manufacturing technologies, a pure ceria foam is a feasible and important improvement. Hence, most of the results in this paper are for a receiver made of pure ceria, with the same porous structure properties. This is still considered a conservative estimate, since dual-scale porosity materials have already been manufactured and demonstrated, with superior volumetric absorption and oxygen exchange capabilities [3,12,47]. A summary of the simulations used in the following analysis is presented in Appendix A.

3.3. Steam flow rate

The effects of the oxidizer flow rate on the oxidation performance are already known, from various experimental works [3]. It is also known that the oxidation step is longer than the reduction step (excluding the longer preheating from ambient to reduction temperature at the first cycle every day), mostly due to the slower oxidation kinetics. In Fig. 7 we present the temperature and reaction rates in the reactor for the first cycle, in a case with a higher steam flow rate. It is seen from this figure that the oxygen release rate peak occurs before the temperature peak, due to the secondary oxidation at the back of the receiver (re-oxidising the ceria by O_2 released from the front), as mentioned in Lidor et al. [37]. We have shown for the standard case that the actual hydrogen production is much smaller than the maximum possible under the achieved reduction extent. In Fig. 9 we present the generated H_2 (m_{H_2}) and H_2 to H_2O conversion extent ($X_{H_2-H_2O}$) as a function of the steam flow rate, for the first cycle in the standard case. It can be seen that the amount of generated hydrogen increases with a higher steam flow rate, but the gradient becomes smaller as the amount of generated hydrogen is getting closer to the maximum limit. At the same time, the mean H_2 to H_2O conversion extent decreases with an increased steam flow rate.

When we study the second cycle for the standard case, a different trend is observed (Fig. 10). The amount of H_2 produced increases with the steam flow rate, however the H_2 to H_2O

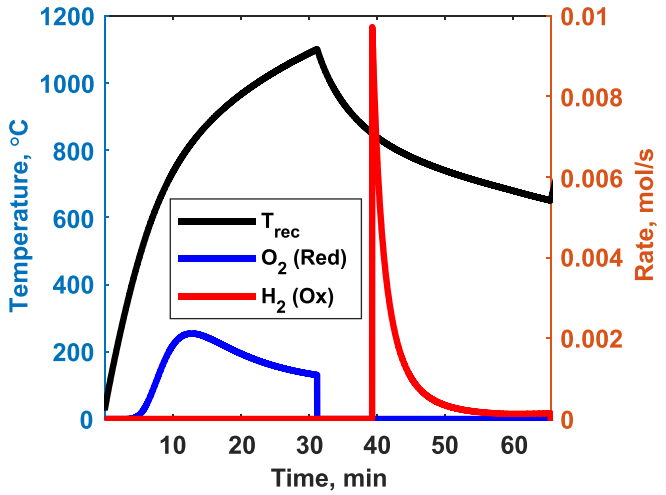

Fig. 7. Receiver mean temperature, O_2 release rate and H_2 production rate for the first cycle in a case with $\dot{m}_{H_2O} = 50$ kg h^{-1}.

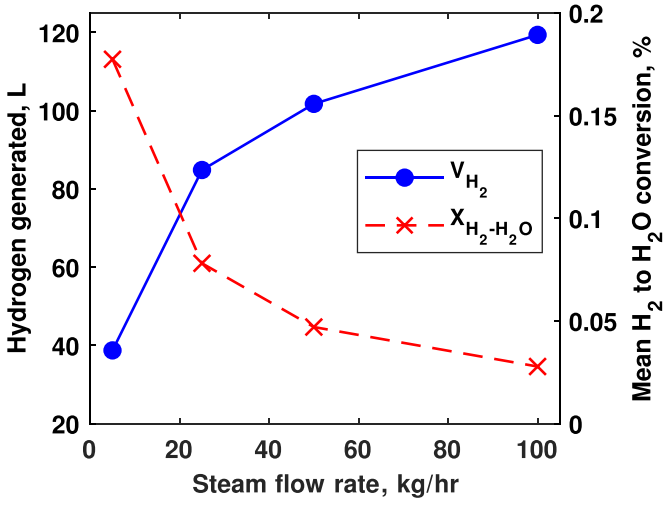

Fig. 9. Amount of hydrogen produced and mean H_2 to H_2O conversion extent as a function of the steam flow rate for the first cycle. $T_{red,\ end} = 1100$ °C, $f_{CeO_2} = 25\%$, $V_{H_2,ideal} = 131.876$ L.

conversion extent peaks at 50 kg h^{-1} and then drops significantly at 100 kg h^{-1}. Moreover, the maximum (ideal) H_2 production changes for the second cycle for each case, since the initial conditions at the beginning of the second cycle are different, unlike the first cycle where the reactor was cold, and the reduction step was identical. Hence, a different amount of oxygen is released during the second cycle reduction step, giving us a different value of the ideal amount of H_2 that can be produced. When we normalize the actual H_2 generated by the ideal H_2 generated and multiply it by the ideal H_2 production of case 1, we can see that the increase in H_2 yield is linear, hinting that there is still a significant increase towards the maximum H_2 yield. This is also supported by Fig. 8 showing that the oxidation rate has not reached its peak, although the mean reactor temperature has reached $T_{ox,\ end}$. In addition to this, the conversion extent is significantly lower than in the first cycle. This can be mitigated to an extent by varying the oxidation step limits ($T_{ox,\ start}$ and $T_{ox,\ end}$).

The same results for the H_2 production rate and total yield, normalized by the ceria mass loading, are presented in Figs. 11 and 12 for 25% and 100% ceria mass fraction. We can see from both of these figures that the second cycle tends to be less efficient than the first cycle. In the following results we will show that the performance of the subsequent cycles can be improved under a better operational scheme. At the same time it is noted that increasing the steam flow rate also increases the energy requirements from the system, calculated by $Q_{steam,\ req} = \dot{m}_{H_2O} t_{ox} (h_{H_2O,in} - h_{H_2O,amb})$. As the latent heat of water is large, this value can affect the system performance. However, the reactor design allows for an efficient and straightforward use of an external heat exchanger, using the heat stored in the outlet stream of H_2/H_2O. In Fig. 13 we present the required energy for the steam generation and the available energy in the outlet stream during the oxidation step. We can see that the available energy is almost identical, and hence a simple counter-current heat exchanger can be used in minimizing the required energy for steam generation to a negligible amount, compared to

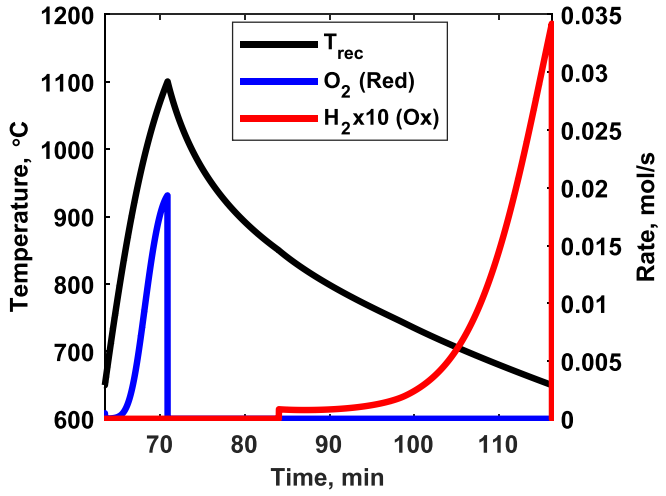

Fig. 8. Receiver mean temperature, O_2 release rate and H_2 production rate for the second cycle in a case with $\dot{m}_{H_2O} = 50$ kg h^{-1}.

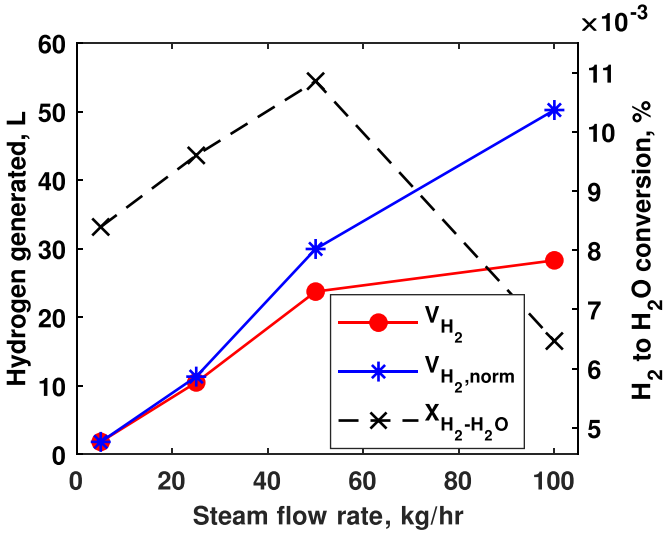

Fig. 10. Amount of hydrogen produced and mean H_2 to H_2O conversion extent as a function of the steam flow rate for the second cycle. $T_{red,\ end} = 1100$ °C, $\varphi_{CeO_2} = 25\%$. $V_{H_2,norm}$ is the amount of hydrogen normalized by the ratio of the ideal H_2 production for each case to the 5 kg h^{-1} case.

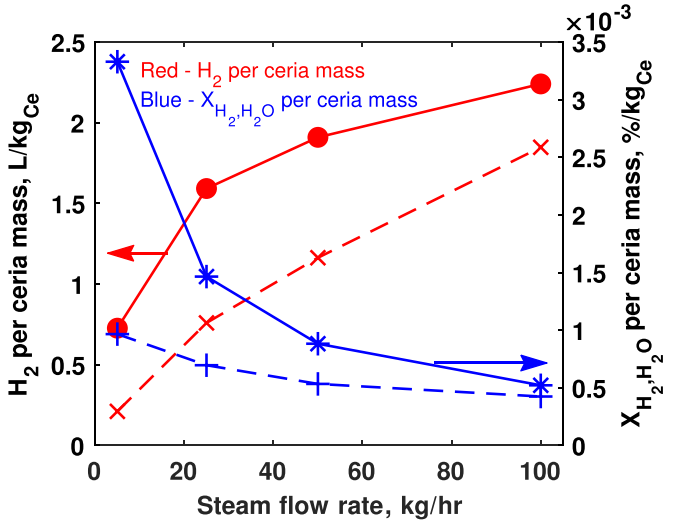

Fig. 11. Generated hydrogen and mean H_2 to H_2O conversion extent normalized per ceria mass as a function of the steam flow rate for the first cycle in Case 1 to Case 4 (solid line: $\varphi_{Ce} = 25\%$, dashed line: $\varphi_{Ce} = 100\%$).

the solar input. We also note that our investigation into using a higher temperature steam did not have any significant effect on the system: the performance in terms of H_2 yield and conversion ratio remained almost identical, with changes of less than 0.1% for a steam inlet temperature of 600 °C. Moreover, larger differences between the required steam energy and the outlet stream available energy were found, with a value of 3936 kJ for 50 kg h^{-1} at $T_{H_2O,in} = 600\circ C$.

3.4. Heat recovery

We have shown that heat recovery during oxidation is feasible, resulting in a small amount of additional energy required for the steam generation in addition to the heat exchanger. However, there is also a significant amount of sensible energy stored in the sweep gas that flows through the reactor during the reduction and cooldown steps. In a previous work [37] we have evaluated the positive effects of a possible heat recovery on the reactor performance, by evaluating its temperature profile and non-stoichiometry extent in cases where the inlet N_2 temperature is higher. With the modified MONROE model we are now able to estimate the feasibility of using the outlet sweep gas for the preheating of the fresh cold sweep gas prior to reaching the inlet. The required heat transfer rate for the preheating is $\dot{Q}_{N_2,req} = \dot{m}_{N_2} c_{p,in}(T_{in} - T_0)$, where T_{in} is the required heat recovery temperature (inlet temperature) and T_0 is the sweep gas supply temperature. By calculating the required heat transfer rate, we can use it, together with the calculated outlet temperature (during the reduction and cooldown steps) to find the maximum possible heat transfer rate at the outlet

$$\dot{Q}_{HR,max} = \dot{m}_{N_2} \int_{T_0}^{T_{out}} c_{p,N_2} dT \tag{12}$$

and the minimum required outlet temperature to from the equation for the required heat transfer rate

$$\dot{Q}_{N_2,req} = \dot{m}_{N_2} \int_{T_0}^{T_{out,\,req}} c_{p,N_2} dT. \tag{13}$$

We have performed an analysis simulating the reactor operation during a full day, assuming total 12 h of sunlight. The required heat transfer rate to preheat the N_2 from ambient temperature to the required $T_{HR} = 600$ °C is 1761.4 W. The heat recovery temperature was selected as 600 °C, since this is an easily feasible value for the current setup (without the need for any special requirements such as ceramic insulation). During the first cycle, starting from a cold reactor, the average available heat transfer rate (Eq. (12)) is 1969.4 W. However, during the fifth cycle the reactor is already hot, and the following cycles become almost identical in terms of temperature profiles, H_2 yield and all other parameters. At this cycle the available heat transfer rate is 4239.3 W, much higher than the required heat transfer rate.

In addition, the required outlet temperature from the reactor during the reduction and cooldown steps is calculated, using Eq. (13). The results are presented in Fig. 14, where we present the

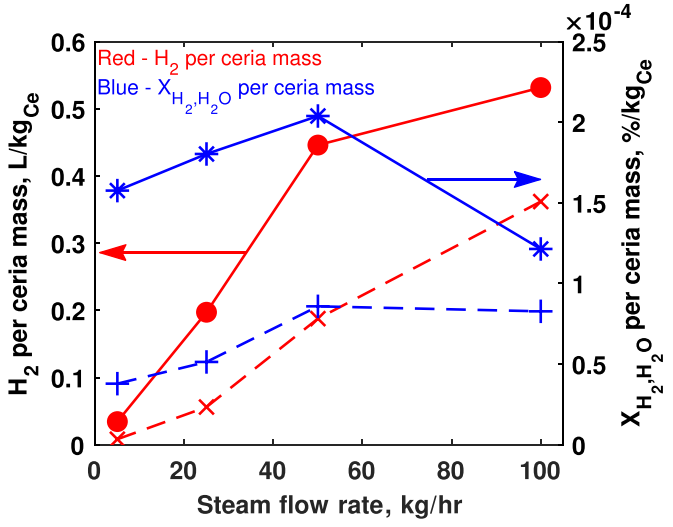

Fig. 12. Generated hydrogen and mean H_2 to H_2O conversion extent normalized per ceria mass as a function of the steam flow rate for the second cycle in Case 1 to Case 4 (solid line: $\varphi_{Ce} = 25\%$, dashed line: $\varphi_{Ce} = 100\%$).

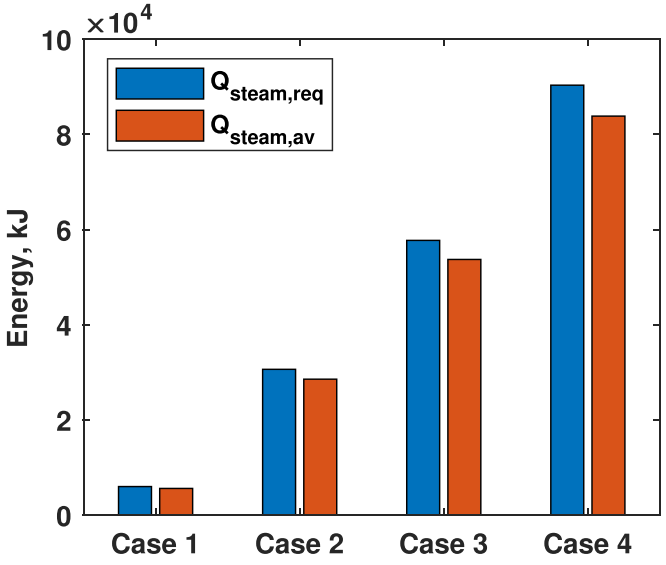

Fig. 13. Energy required for steam generation compared to energy available in the H_2/H_2O mixture at outlet, for case 1–4.

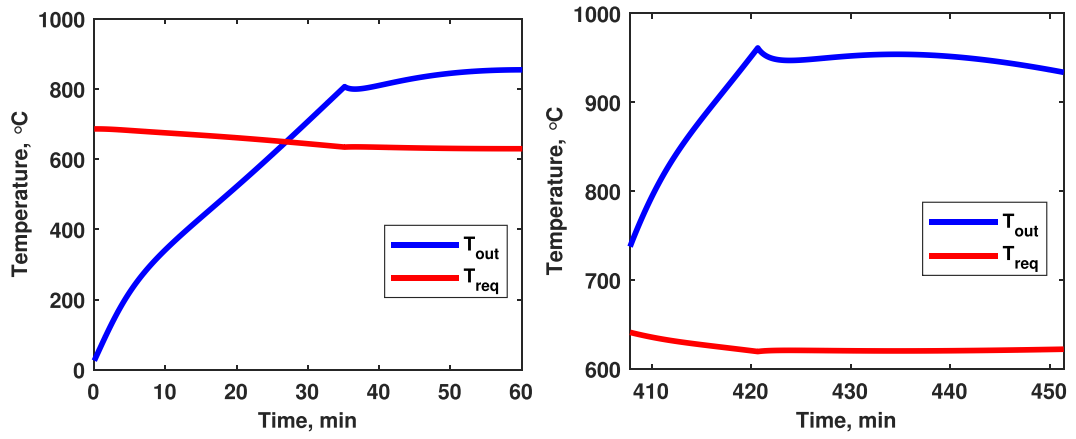

Fig. 14. The required outlet temperature (red) compared to the actual outlet temperature (blue) for: (a) the first cycle; and (b) fifth cycle (Case 5).

calculated outlet temperature and the minimum required outlet temperature for the first cycle and for the fifth cycle. We can see from Fig. 14a that in the first 27 min, the outlet temperature is lower than the required temperature for a complete preheating of the cold N_2 to the required temperature before the reactor inlet. However, once the reactor is heated up during the first cycle, the outlet N_2 temperature remains higher than the minimum required value. Even though theoretically, the excess energy during all the cycles past the first can be used as well, we do not pursue this further in the scope of this work. For our purpose, we show that implementing a heat exchanger at the reactor outlet/inlet is a simple task, boosting the performance due to the higher inlet temperature. This is possible also for temperatures above 600 °C. A potential improvement can be the addition of a thermal energy storage (TES) unit to the system, recovering this excess heat for using in a nitrogen purification process, thus boosting the efficiency, or in another industrial process requiring thermal energy. Such a setup, including both heat recovery and thermal energy storage unit, is presented in Fig. 15. In this setup, the excess high−temperature heat stored in the warm N_2− O_2 outlet stream is fed into a thermocline−based TES unit, which can be based on a sensible or combined sensible/latent concept [55]. Usually, these units consist of a packed−bed configuration, in which the specific material and geometric design are based on the expected fluid temperature, type and flow rate. By flowing the high−temperature fluid through them, the heat is transferred to the storage medium, and the fluids leaves the TES unit at ambient temperature. The stored energy can then be extracted upon demand, by switching the flow direction, entering with a cold heat transfer fluid from the cold side, heating it and leaving the TES unit at the storage temperature. Another interesting approach for the utilization of the remaining heat is using it in a nitrogen purification unit. Since one of the energy penalties in the operation of a sweep gas−operated solar reactor is the required energy for the oxygen removal from the sweep gas during reduction, the remaining heat in the warm N_2− O_2 outlet stream can be used in a low−temperature redox

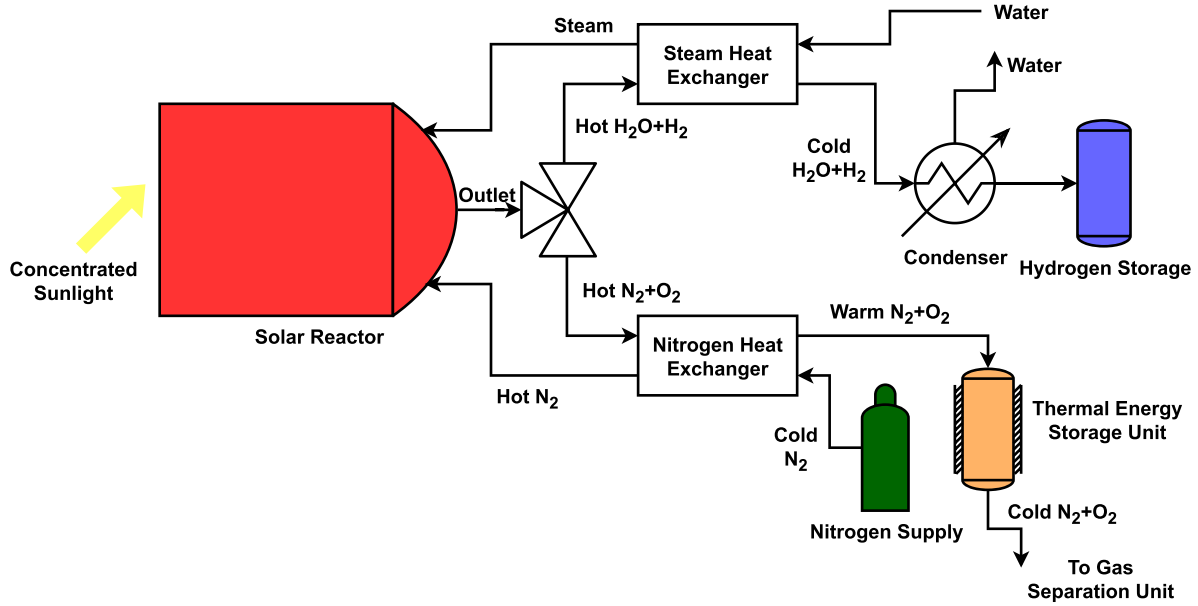

Fig. 15. System flowchart with heat recovery for both N_2 and steam lines and thermal energy storage unit.

chemical looping process for nitrogen purification [56]. A detailed analysis of any of these options is outside the scope of this work.

An additional improvement that was investigated is the use of different sweep gas flow rates during different stages of the reduction and cooldown steps. Since the significant oxygen release only starts at higher temperatures, the reactor can be operated with a very low N_2 flow during the first part of the reduction. Once the temperature is high enough, the N_2 flow rate changes to the normal rate needed for properly sweeping the released oxygen and keeping the O_2 partial pressure low for favourable reduction conditions. When the receiver reaches the target reduction temperature and the cooldown step begins, we can lower again the N_2 flow rate, until the oxidation step begins and the flow changes from sweep gas to steam. The major benefit of this approach is that it can significantly reduce one of the parasitic energy losses, the required energy for oxygen removal from the inert sweep gas, which has been identified as a significant loss [27]. The effects were studied for reducing the sweep gas flow rate both during the reduction and cooldown steps, with the reduced flow rate set to $\dot{m}_{N_2,low} = 0.01\ kg\,s^{-1}$. We have discovered that starting the sweep gas flow late in the reduction step, even at $T_{rec,\,avg} = 1100\ ^{\circ}C$, does not have a significant effect on the cycle performance. The solar to fuel efficiency is slightly increased (from 3.8068% to 4.1035%), due to the lower amount of inert gas requiring separation, while at the same time the total amount of hydrogen produced is decreased from 127.137 g to 127.128 g per cycle (more detailed results are presented in the supplementary).

3.5. Energy balance analysis

We have also analysed the instantaneous energy balance during the reduction step, since this is the most energy intensive step in the cycle. The following energy terms have been calculated: re-radiation losses from the reactor, sensible heat of the shell and insulation, energy consumed by the chemical reaction, sensible heat change in the receiver, and the sweep gas fluid sensible heat. In Fig. 16a we present the energy balance over the reduction step of the first cycle, when the reactor starts from ambient temperature. We can see that the re-radiation losses increase from almost negligible fraction of the total incoming solar power to 88.6%. The receiver sensible heat, starting from accounting for almost all the incoming solar power, ends at 9.74% in the end of the reduction step. In average, the receiver sensible heat accounts for 35.3% of the total energy, while the re-radiation losses accounts for 63.89%. The shell and insulation sensible heat accounts on average for 0.82%, while sweep gas sensible heat and chemical reaction energy are negligible.

During the second cycle, a different energy balance trend is evident (Fig. 16b). The re-radiation losses begin as 5% of the solar power, but they only reach 68% by the end of reduction. The sensible heat in the receiver starts at 94% of the solar power at the beginning of the reduction step, and ends at 29%. When looking at the average values, the re-radiation losses account for 40.3% of the total solar energy input while the receiver sensible heat is 57.39%. Since the reduction step during the second cycle is shorter, the total solar energy is smaller, and the average sensible heat of the shell and insulation increases to 2.32%, with the chemical reaction and sensible heat of the fluid still negligible (less than 0.001%). Interestingly, the general distribution of the energy to the various terms remains quite similar for the more advanced runs with the same absorber thickness (case 6), but are slightly modified when the absorber thickness is reduced to 30 mm (case 7). The first cycle in case 7 shows that the re-radiation losses are 58.7%, with the receiver sensible heat using 34.1% of the total solar energy. The shell and insulation sensible heat increases to 7.2%, with the chemical reaction and fluid sensible heat still below 0.1% each. However, looking at the fifth cycle in case 7 (when the change between consecutive cycles is negligible), the re-radiation losses slightly reduces to 55.9% and the receiver sensible heat increases to 36.2%. The shell and insulation sensible heat is 7.83% of the total solar energy and the chemical reaction energy and fluid sensible heat remains below 0.01%. The difference between the first and later cycles in the case of a thinner receiver is not as significant as in the other cases, where the receiver is 60 mm thick.

The main conclusion from the energy balance is that re-radiation losses remain dominant in all cases. Only during the first cycle of case 1 are the receiver sensible heat losses greater than the re-radiation losses. Hence, it is of utmost importance to try and mitigate these losses. The straightforward solution is decreasing the aperture size. However, this can only be done if the concentrating system can still deliver the required solar power into the cavity, and it might decrease the solar field efficiency. Another noteworthy observation is that increasing the solar power does not increase the percentage of the re-radiation losses (of course the total solar energy might increase as a result, although higher solar power results in a shorter reduction step). This is since the re-radiation losses are only linearly dependant on the solar power, and we observe a similar trend with the receiver sensible heat. In

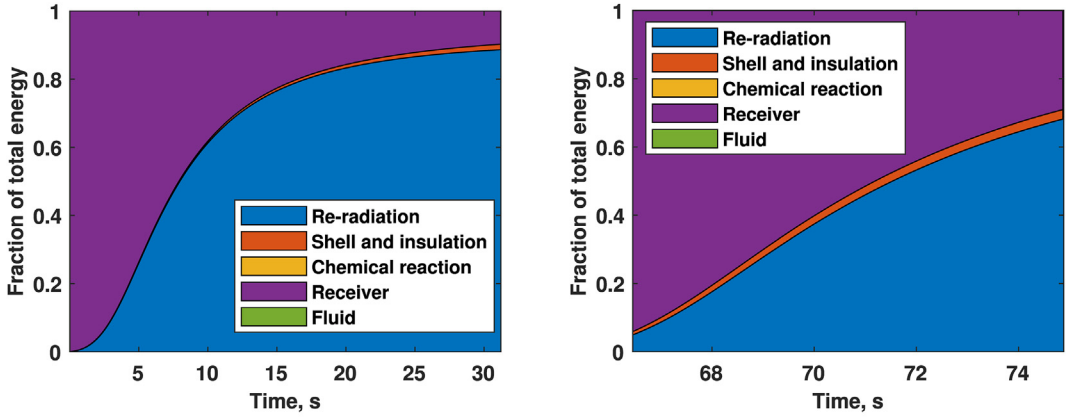

(a) First cycle (b) Second cycle

Fig. 16. The energy balance on the reactor during the reduction step for the standard case (case 1): (a) first cycle; (b) second cycle.

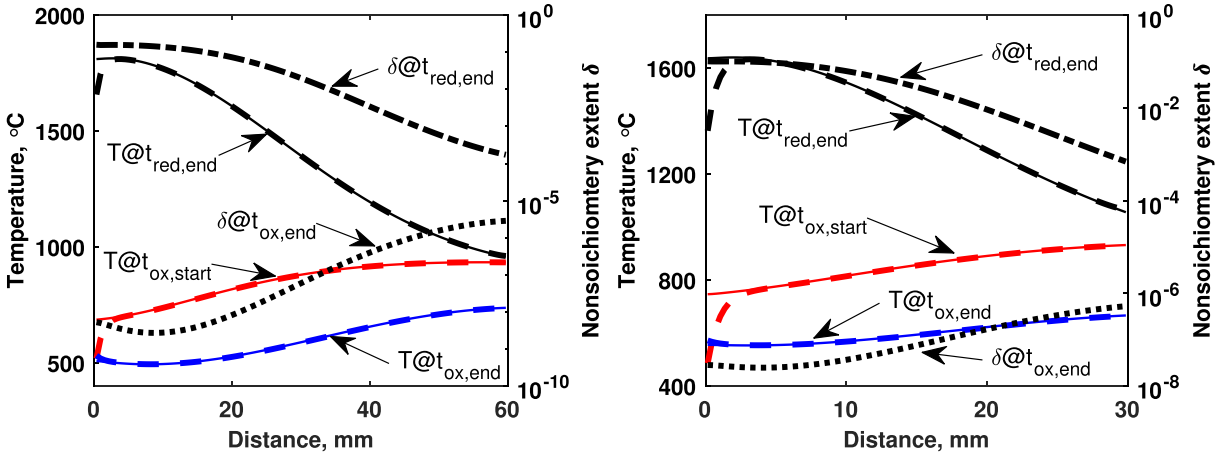

Fig. 17. The temperature (solid lines for T_s, dashed lines for T_f) and nonstoichiomtery extent profiles across the receiver for $T_{red,\ avg} = 1400$ °C for advanced cycles (cycle 4). (a) $t_{rec} = 60$ mm (case 6); and (b) $t_{rec} = 30$ mm (case 7).

comparison, the re-radiation losses are proportional to the average receiver temperature in the power of 4. That is why an increase in the receiver temperature at the reduction step end has a higher effect on the fraction of the re-radiation losses from the total energy, as well as on the overall required solar energy.

3.6. Reactor performance

The absorber thickness is a critical parameter, as was shown in our previous work [37], as well as for other volumetric solar reactors [37,57]. While in theory a thicker receiver increases the ceria mass loading, we have seen that several issues arise from this. First, the radiation is absorbed in the first few millimetres of the material, causing a large temperature gradient over the receiver, with a higher peak temperature at the front, and lower temperature at the back, as is seen in Fig. 17a. This in turn causes a lower reduction extent. However, since the reduction extent of ceria is not a linear function of temperature, the overall oxygen release will still be greater than that for a thinner receiver (lower ceria mass loading). In Fig. 17b we present the same temperature and nonstoichiometry extent profiles for a thinner receiver. We show that not only the temperature gradient is smaller than for the thicker receiver, but also that the extent of reduction reached in most of the receiver is higher. However, due to the nature of the dependency of the nonstoichiomtery extent on the temperature, the front of the receiver has a much larger δ in the case of the thick receiver.

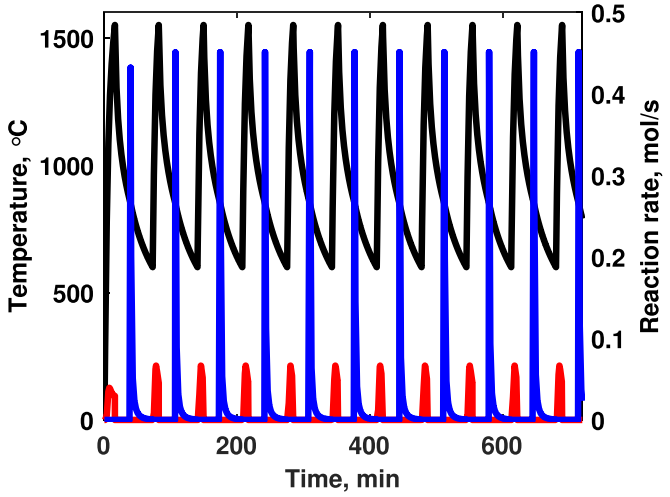

Fig. 18. Mean receiver temperature and reduction and oxidation reaction rates for a full day run (12 h) - Case 8. Black - average receiver temperature $T_{rec,\ avg}$, blue - H_2 reaction rate r_{H_2}, red - O_2 reaction rate r_{O_2}.

Up to this point we have analysed the systems behaviour and the effects of several key parameters in its performance. To evaluate the performance and full potential of the solar reactor, we now present results for a complete setup operating over a full day. We assume that there are 12 h of operational time, with constant radiative flux. Due to the ratio between the different steps, three reactors can be mounted on the same solar tower or dish, using the same concentrating system. In Fig. 18 we present the average receiver temperature and reaction rates of O_2 release and H_2 production, over the complete run. In our analysis, we have assumed that after 12 h, if the system has finished reduction and is at the cooldown or oxidation steps, it can finish the current cycle, since no solar power is required after the reduction step. If the system is only partially reduced, it can be still be oxidised with steam to generate some hydrogen, while cooling down the reactor. Results for three sample cases are presented in Table 5 (the initial and boundary conditions are specified in Appendix A). The cases analysed are for different absorber thickness values, with all other conditions identical (except $T_{red,\ end}$ due to the temperature gradient over various thickness as discussed before). The solar to fuel efficiency is calculated for three cases: (a) where no heat recovery is performed; (b) standard heat recovery, where a heat exchanger is placed at the reactor inlet/outlet with the goal of minimizing the required heat for the N_2 preheating and steam generation (assuming the hot steam outlet must remain as a vapour); and (c) the ideal heat recovery, where the complete steam outlet heat is utilized. Also, the chosen input parameters have all been taken as feasible values for the ASTOR reactor, without pushing the system boundaries (without using very high solar fluxes, extreme heat recovery temperatures or using any other parameter with a value which is very hard to achieve).

First, we note that the total amount of released oxygen is almost identical in all cases, even under different ceria mass loadings. The main reason for this is of course the temperature gradient across

Table 5
Summary of results.

Parameter	Symbol	Unit	Case 6	Case 10	Case 7
Ceria mass	m_{Ce}	kg	213.06	153.07	97.69
Number of full cycles per day	n_{cycles}		8	9	11
Average reduction temperature	$T_{red,\ avg}$	◦C	1400	1450	1550
Maximum reduction temperature	$T_{red,\ max}$	◦C	1813	1777	1745
Reduction step duration	t_{red}	min	12.83	9.983	9.18
Cooldown step duration	t_{cd}	min	30.72	26.88	25
Oxidation step duration	t_{ox}	min	54.43	43.13	33.33
Oxygen released	$V_{O_2,tot}$	L	5252	4938	5028
Hydrogen produced	$m_{H_2,gen}$	kg	1.0396	0.9402	0.8930
Maximum H_2 produced (per day)	$m_{H_2,max}$	kg	1.2043	0.9994	1.0103
Hydrogen production (3 reactors)	$m_{H_2,tot}$	kg	3.1188	2.8207	2.6790
Total inert gas separation energy	$Q_{inert,\ tot}$	kJ	68748	51549	54889
Hydrogen to oxygen ratio	$n_{H_2-O_2}$		1.9286	1.8786	1.7841
Average H2O to H2 conversion	$X_{H_2O-H_2,avg}$	%	0.69714%	0.69290%	0.64015%
Solar to fuel efficiency	η_{sf}	%	3.8099%	4.0454%	3.8483%
Solar to fuel efficiency (HR)	$\eta_{sf,HR}$	%	5.4108%	5.8620%	5.3412%
Solar to fuel efficiency (ideal)	$\eta_{sf,\ ideal}$	%	17.0498%	21.1617%	15.7675%

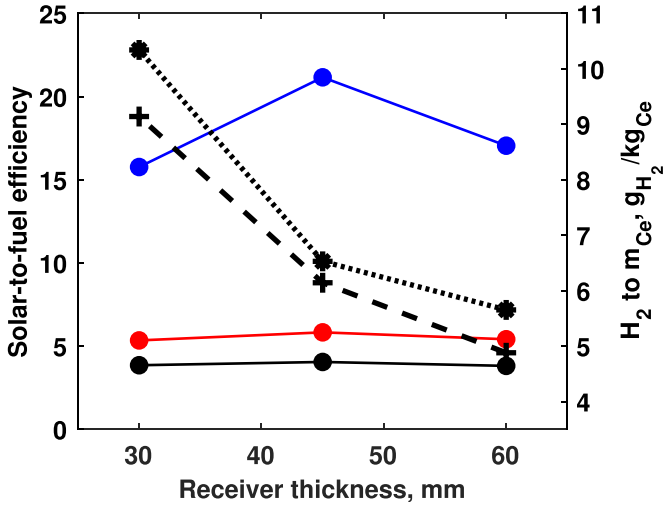

Fig. 19. Solar to fuel efficiency (black - normal η_{sf}, red - with heat recovery $\eta_{sf,HR}$, blue - ideal $\eta_{sd,\ ideal}$) and H_2 produced per ceria mass loading (dashed - actual, dotted - maximum) versus the absorber thickness.

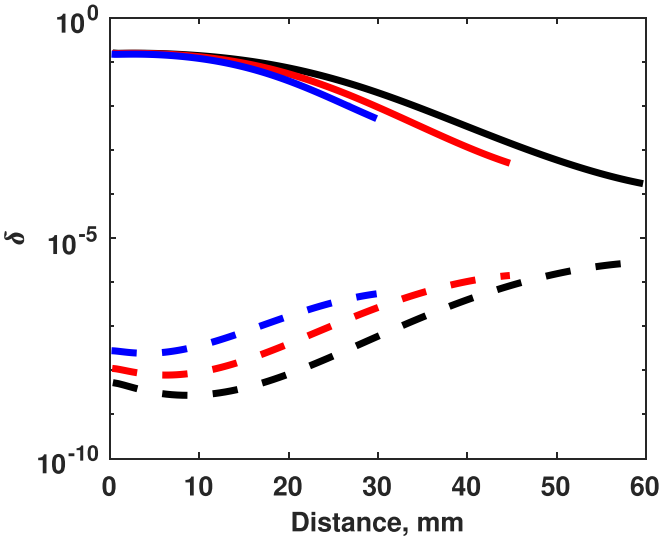

Fig. 20. Nonstoichiomtery extent profiles across the receiver for various absorber thickness at the start and end of the reduction step (solid lines - reduction end, dashed lines - reduction start). Black - absorber thickness 60 mm, red - absorber thickness 45 mm, blue - absorber thickness 30 mm.

the receiver, as discussed previously. However, the overall conclusion about the system performance is more complex than just the extent of reduction achieved, as discussed in the following paragraphs. The number of full cycles includes the last cycle which ends after the 12 h period as described previously, and when this cycle did not include full reduction, it is noted. For the last oxidation step, a conservative estimate is that oxidation occurs only until $T_{ox,\ end}$ and not until full re-oxidation of the ceria, as the low temperature oxidation might be slow and inefficient. As expected, the maximum temperature in the receiver $T_{red,\ max}$ is inverse to the mean temperature $T_{red,\ avg}$ for the three cases, due to the thickness of the material. In terms of the total hydrogen production, the highest ceria mass loading has the largest value. However, the increase is not proportional to the ratio in the mass loading. In Fig. 19 we present the solar to fuel efficiency and produced hydrogen over the ceria mass loading against the absorber thickness. The lowest efficiency curve presented in Fig. 19 is the normal calculated solar to fuel efficiency, without any heat recovery (black solid line). The highest efficiency, 4.05%, is for the medium sized reactor with absorber thickness of 45 mm (corresponding to ceria mass loading of 157.07 kg). This trend is kept for the efficiency with heat recovery ($\eta_{sf,HR}$ = 5.86%) as well as in the ideal case ($\eta_{sf,\ ideal}$ = 21.16%), hinting that the optimum absorber thickness in terms of efficiency lies within the range we explored. It is also shown in this figure that the highest mass of generated hydrogen per ceria mass loading if for the 30 mm receiver, while the lowest value is found to be for the 60 mm thick receiver. The 45 mm thick receiver shows the smallest difference between the actual and ideal values of H_2 produced per ceria mass. In general, the behaviour of the H_2 yield per CeO_2 mass is proportional to the absorber thickness.

The extent of reduction across the receiver is presented in Fig. 20, showing the δ values at the start and end of the reduction step for all three cases. It is shown that for the thicker receiver, the non-stoichiometry extent at the reduction start is lower compared to the thinner receivers, mostly due to the longer oxidation step. This allows for more hydrogen to be produced per cycle with a thicker receiver. However, part of the reason for the lower hydrogen generated per ceria mass loading is due to the unwanted reduction at the receiver back. As discussed before, during the beginning of the oxidation the largest amount of hydrogen is produced. This

Table 6
Summary of effects of system parameters.

Parameter	Positive effects	Negative effects	Other effects
Increasing φ_{Ce}	higher $m_{H_2,gen}$	none	slight changes in material properties
Increasing $\dot{m}_{steam}$	higher $m_{H_2,gen}/m_{Ce}$	lower $X_{H_2-H_2O}$, lower η_{sf}	drop in η_{sf} can be mitigated by heat recovery
Increasing L	higher $m_{H_2,gen}$	higher $T_{red,\ max}$, larger temperature gradient over receiver	
Increasing $T_{N_2,start}$	lower Q_{inert}, higher η_{sf}	negligible reduction in $m_{H_2,gen}$, slightly longer t_{red}	
Increase T_{HR}	higher $\eta_{sf,HR}$, shorter t_{red}	slightly increased preheating energy	requires heat exchanger at inlet/outlet

hydrogen can cause some reduction to occur at the back of the receiver, where the ceria is not significantly reduced. Thus, some of the generated hydrogen is converted back to steam, decreasing the conversion extent and lowering the reactor performance.

Summarizing the results, it is clear that there is an optimum point for the reactor performance. However, the optimum point might differ based on the performance metric we are trying to optimise. In Table 6 we present a summary of the effects we have presented in this work for the various operational parameters.

4. Conclusions

We have investigated various advanced concepts in the design and operation of a solar receiver–reactor for hydrogen production by the 2-step redox cycle, operated with a sweep gas. By using the modified MONROE code, we identified the major challenges that limit the hydrogen production of this type of reactor, and have thoroughly analysed the various solutions that can be implemented to significantly improve the reactor performance and hydrogen yield. The main conclusions that are drawn from this work are as follows:

1. The planned steam flow rate of 5 kg h^{-1} is too low for a significant hydrogen yield. A larger flow rate is required in order to increase the hydrogen production and reach values closer to the maximum possible yield. Even though this will decrease the conversion extent, the objective of such reactor is hydrogen production. We have also seen that the available energy in the outlet stream is almost identical to the required energy for the steam generation, so that increasing the mass flow rate to 100 kg h^{-1} is a promising method for increasing the reactor performance with minimal drawbacks.
2. A simple heat recovery system, using gas-gas and vaporizer types heat exchangers at the inlet/outlet manifold, can increase the solar to fuel efficiency of the reactor above 5%. A more thorough but complex heat recovery scheme can increase this value for up to 21.16% in some cases. This value is an ideal limit for such a reactor, but one that is based on physical modelling of the transient behaviour of the system and with conservative estimations, unlike general thermodynamic analysis, which tends to predict theoretical efficiency values in excess of 30% which cannot be reached in practice due to technical limitations.
3. A volumetric solar reactor operated with a sweep gas is a complex system in terms of all the physical phenomena occurring in parallel during its operation. We show that isolating the effect of every single parameter is not a straightforward task. Moreover, in many cases one parameter has conflicting effects on different performance metrics. The modified MONROE code can be used to perform a detailed parametric sweep of the key parameters, using hundreds of various combinations, to generate performance maps that can be combined with optimization techniques for finding the optimum points.
4. The total hydrogen yield improves with increased absorber thickness. While the solar to fuel efficiency and normalized hydrogen yield per ceria mass are decreased with an increase in thickness, an array of three solar reactors with a 60 mm receiver has the potential to generate 3 kg of hydrogen per day under feasible conditions. However, it is noted that for a thick receiver to be able to reach these goals, the maximum temperature inside will be higher than for a thinner receiver, and will result in a larger temperature gradient across the receiver. This can lead to mechanical degradation of the receiver, and must be taken into account when constructing or upgrading such a large scale reactor.
5. Since re-radiation and sensible heat are the dominant energy terms during the reactor operation, identical to the trends shown for vacuum-operated solar redox reactors, any improvements in these aspects can benefit both types of reactors. A possible method for improving the solar to fuel efficiency might be to add a shutter to the reactor, closing the aperture at the end of the reduction, and flowing nitrogen at a large flow rate through the reactor cavity in order to shorten the cooldown phase while recovering the sensible heat. This recovered heat can be stored in a thermal energy storage unit and be used at the plant.

CRediT authorship contribution statement

A. Lidor: Conceptualization, Methodology, Software, Validation, Formal analysis, Investigation, Data curation, Writing – original draft, Writing – review & editing, Funding acquisition. **T. Fend:** Conceptualization, Writing – review & editing, Project administration. **M. Roeb:** Project administration, Funding acquisition. **C. Sattler:** Project administration, Funding acquisition.

Declaration of competing interest

The authors declare that they have no known competing financial interests or personal relationships that could have appeared to influence the work reported in this paper.

Acknowledgements

This project has received funding from the European Union's Horizon 2020 research and innovation programme under the Marie Sklodowska-Curie grant agreement No 832535. It was also supported by the European Regional Development Fund and the NRW-Ministry of Economic Affairs, Innovation, Digitalisation and Energy in the framework of project ASTOR (EFRE-0800877).

Appendix A. Results Summary

In this appendix the initial and boundary conditions of the various runs used in this work are described in Tables A.1 and A.2 (changes in parameters are emphasized).

Table A.1
Summary of input data for different cases (part 1)

Parameter	Case 1	Case 2	Case 3	Case 4	Case 5
Absorber thickness L	0.06 m	0.06 m	0.06 m	0.06 m	0.06 m
Ceria mass fraction φ_{Ce}	25%	25%	25%	25%	**100%**
Inlet N_2 temperature T_{in,N_2}	25 °C	25 °C	25 °C	25 °C	**600 °C**
Inlet steam temperature T_{in,H_2O}	150 °C	150 °C	150 °C	150 °C	150 °C
N_2 mass flow $\dot{m}_{N_2}$	20 kg h^{-1}	20 kg h^{-1}	20 kg h^{-1}	20 kg h^{-1}	20 kg h^{-1}
Steam mass flow $\dot{m}_{H_2O}$	**5 kg h^{-1}**	**25 kg h^{-1}**	**50 kg h^{-1}**	**100 kg h^{-1}**	100 kg h^{-1}
Solar power q	150 kW	150 kW	150 kW	150 kW	**250 kW**
Reduction end temperature $T_{red,\ end}$	1100 °C	1100 °C	1100 °C	1100 °C	**1400 °C**
Oxidation start temperature $T_{ox,\ start}$	850 °C	850 °C	850 °C	850 °C	850 °C
Oxidation end temperature $T_{ox,\ end}$	650 °C	650 °C	650 °C	650 °C	**600 °C**
N_2 starting temperature $T_{N_2,start}$	25 °C	25 °C	25 °C	25 °C	25 °C

Table A.2
Summary of input data for different cases (part 2).

Parameter	Case 6	Case 7	Case 8	Case 9	Case 10
Absorber thickness L	0.06 m	**0.03 m**	0.03 m	**0.06 m**	**0.045 m**
Ceria mass fraction φ_{Ce}	100%	100%	100%	100%	100%
Inlet N_2 temperature T_{in,N_2}	600 °C	600 °C	**800 °C**	600 °C	600 °C
Inlet steam temperature T_{in,H_2O}	150 °C	150 °C	150 °C	150 °C	150 °C
N_2 mass flow $\dot{m}_{N_2}$	20 kg h^{-1}	20 kg h^{-1}	20 kg h^{-1}	20 kg h^{-1}	20 kg h^{-1}
Steam mass flow $\dot{m}_{H_2O}$	100 kg h^{-1}	100 kg h^{-1}	100 kg h^{-1}	100 kg h^{-1}	100 kg h^{-1}
Solar power q	250 kW	250 kW	250 kW	250 kW	250 kW
Reduction end temperature $T_{red,\ end}$	1400 °C	1400 °C	1400 °C	**1550 °C**	**1500 °C**
Oxidation start temperature $T_{ox,\ start}$	850 °C	850 °C	850 °C	850 °C	850 °C
Oxidation end temperature $T_{ox,\ end}$	600 °C	600 °C	600 °C	600 °C	600 °C
N_2 starting temperature $T_{N_2,start}$	600 °C	600 °C	**1100 °C**	**1100 °C**	600 °C

Appendix B. Supplementary data

Supplementary data to this article can be found online at https://doi.org/10.1016/j.renene.2021.07.089.

References

[1] C. Agrafiotis, M. Roeb, C. Sattler, 4.18 solar fuels, in: Comprehensive Energy Systems, Elsevier, 2018, pp. 733–761, https://doi.org/10.1016/B978-0-12-809597-3.00429-6.

[2] B. Bulfin, J. Vieten, C. Agrafiotis, M. Roeb, C. Sattler, Applications and limitations of two step metal oxide thermochemical redox cycles; a review, J. Mater. Chem. 5 (36) (2017) 18951–18966, https://doi.org/10.1039/C7TA05025A.

[3] D. Marxer, P. Furler, M. Takacs, A. Steinfeld, Solar thermochemical splitting of CO_2 into separate streams of CO and O_2 with high selectivity, stability, conversion, and efficiency, Energy Environ. Sci. 10 (5) (2017) 1142–1149, https://doi.org/10.1039/C6EE03776C.

[4] Y. Lu, L. Zhu, C. Agrafiotis, J. Vieten, M. Roeb, C. Sattler, Solar fuels production: two-step thermochemical cycles with cerium-based oxides, Prog. Energy Combust. Sci. 75 (2019) 100785, https://doi.org/10.1016/j.pecs.2019.100785.

[5] M. Tou, R. Michalsky, A. Steinfeld, Solar-driven thermochemical splitting of CO_2 and in situ separation of CO and O_2 across a ceria redox membrane reactor, Joule 1 (1) (2017) 146–154, https://doi.org/10.1016/j.joule.2017.07.015.

[6] M. Hoes, C.L. Muhich, R. Jacot, G.R. Patzke, A. Steinfeld, Thermodynamics of paired charge-compensating doped ceria with superior redox performance for solar thermochemical splitting of H_2O and CO_2, J. Mater. Chem. 5 (36) (2017) 19476–19484, https://doi.org/10.1039/C7TA05824A.

[7] B. Bulfin, M. Lange, L. de Oliveira, M. Roeb, C. Sattler, Solar thermochemical hydrogen production using ceria zirconia solid solutions: efficiency analysis, Int. J. Hydrogen Energy 41 (42) (2016) 19320–19328, https://doi.org/10.1016/j.ijhydene.2016.05.211.

[8] M. Roeb, M. Neises, J.-P. Säck, P. Rietbrock, N. Monnerie, J. Dersch, M. Schmitz, C. Sattler, Operational strategy of a two-step thermochemical process for solar hydrogen production, Int. J. Hydrogen Energy 34 (10) (2009) 4537–4545, https://doi.org/10.1016/j.ijhydene.2008.08.049.

[9] M. Roeb, J.-P. Säck, P. Rietbrock, C. Prahl, H. Schreiber, M. Neises, L. de Oliveira, D. Graf, M. Ebert, W. Reinalter, M. Meyer-Grünefeldt, C. Sattler, A. Lopez, A. Vidal, A. Elsberg, P. Stobbe, D. Jones, A. Steele, S. Lorentzou, C. Pagkoura, A. Zygogianni, C. Agrafiotis, A. Konstandopoulos, Test operation of a 100kW pilot plant for solar hydrogen production from water on a solar tower, Sol. Energy 85 (4) (2011) 634–644, https://doi.org/10.1016/j.solener.2010.04.014.

[10] J.-P. Säck, M. Roeb, C. Sattler, R. Pitz-Paal, A. Heinzel, Development of a system model for a hydrogen production process on a solar tower, Sol. Energy 86 (1) (2012) 99–111, https://doi.org/10.1016/j.solener.2011.09.010.

[11] A. Vidal, A. Gonzalez, T. Denk, A 100 kW cavity-receiver reactor with an integrated two-step thermochemical cycle: thermal performance under solar transients, Renew. Energy 153 (2020) 270–279, https://doi.org/10.1016/j.renene.2020.01.146.

[12] R. Schäppi, D. Rutz, P. Basler, A. Muroyama, P. Haueter, P. Furler, A. Steinfeld, Solar thermochemical splitting of CO_2 in a modular solar dish-reactor system, in: Proceedings of the ISES Solar World Congress 2019 and IEA SHC International Conference on Solar Heating and Cooling for Buildings and Industry 2019, International Solar Energy Society, 2019, pp. 1405–1408, https://doi.org/10.18086/swc.2019.24.08.

[13] D. Marxer, P. Furler, J. Scheffe, H. Geerlings, C. Falter, V. Batteiger, A. Sizmann, A. Steinfeld, Demonstration of the entire production chain to renewable kerosene via solar thermochemical splitting of H_2O and CO_2, Energy Fuel. 29 (5) (2015) 3241–3250, https://doi.org/10.1021/acs.energyfuels.5b00351.

[14] S. Lorentzou, D. Dimitrakis, A. Zygogianni, G. Karagiannakis, A.G. Konstandopoulos, Thermochemical H_2O and CO_2 splitting redox cycles in a $NiFe_2O_4$ structured redox reactor: design, development and experiments in a high flux solar simulator, Sol. Energy 155 (2017) 1462–1481, https://doi.org/10.1016/j.solener.2017.07.001.

[15] B.J. Hathaway, R. Bala Chandran, A.C. Gladen, T.R. Chase, J.H. Davidson, Demonstration of a solar reactor for carbon dioxide splitting via the isothermal ceria redox cycle and practical implications, Energy Fuel. 30 (8) (2016) 6654–6661, https://doi.org/10.1021/acs.energyfuels.6b01265.

[16] T.C. Davenport, C.K. Yang, C.J. Kucharczyk, M.J. Ignatowich, S.M. Haile, Maximizing fuel production rates in isothermal solar thermochemical fuel production, Appl. Energy 183 (2016) 1098–1111, https://doi.org/10.1016/j.apenergy.2016.09.012.

[17] R.B. Diver, J.E. Miller, N.P. Siegel, T.A. Moss, Testing of a CR5 solar thermochemical heat engine prototype, in: ASME 2010 4th International Conference on Energy Sustainability, vol. 2, ASMEDC, 2010, pp. 97–104, https://doi.org/10.1115/ES2010-90093.

[18] E. Koepf, W. Villasmil, A. Meier, Pilot-scale solar reactor operation and characterization for fuel production via the Zn/ZnO thermochemical cycle, Appl. Energy 165 (2016) 1004–1023, https://doi.org/10.1016/j.apenergy.2015.12.106.

[19] M. Tou, J. Jin, Y. Hao, A. Steinfeld, R. Michalsky, Solar-driven co-thermolysis of CO_2 and H_2O promoted by *in situ* oxygen removal across a non-stoichiometric ceria membrane, Reaction Chemistry & Engineering 4 (8) (2019) 1431–1438, https://doi.org/10.1039/C8RE00218E.

[20] N. Gokon, T. Mataga, N. Kondo, T. Kodama, Thermochemical two-step water splitting by internally circulating fluidized bed of NiFe2O4 particles: successive reaction of thermal-reduction and water-decomposition steps, Int. J. Hydrogen Energy 36 (8) (2011) 4757–4767, https://doi.org/10.1016/j.ijhydene.2011.01.076.

[21] T. Kodama, N. Gokon, H.S. Cho, S. Bellan, K. Matsubara, K. Inoue, Particle

fluidized bed receiver/reactor with a beam-down solar concentrating optics: performance test of two-step water splitting with ceria particles using 30-kWth sun-simulator, AIP Conference Proceedings 2033 (2017), https://doi.org/10.1063/1.5067143.
[22] P. Estera, B. Grzegorz, B. Paulina, F. Mariusz, Research on high-Temperature heat receiver in concentrated solar radiation system, EPJ Web Conf. 143. doi:10.1051/epjconf/201714302096.
[23] R. Pitz-Paal, Concept and status of concentrating solar power systems, EPJ Web Conf. 189. doi:10.1051/epjconf/201818900008.
[24] C. Agrafiotis, M. Roeb, C. Sattler, A review on solar thermal syngas production via redox pair-based water/carbon dioxide splitting thermochemical cycles, Renew. Sustain. Energy Rev. 42 (2015) 254–285, https://doi.org/10.1016/j.rser.2014.09.039.
[25] C.L. Muhich, B.D. Ehrhart, I. Al-Shankiti, B.J. Ward, C.B. Musgrave, A.W. Weimer, A review and perspective of efficient hydrogen generation via solar thermal water splitting, Wiley Interdisciplinary Reviews: Energy Environ. 5 (3) (2016) 261–287, https://doi.org/10.1002/wene.174.
[26] E.A. Fletcher, R.L. Moen, Hydrogen- and oxygen from water, Science 197 (4308) (1977) 1050–1056, https://doi.org/10.1126/science.197.4308.1050.
[27] B. Bulfin, F. Call, M. Lange, O. Lübben, C. Sattler, R. Pitz-Paal, I.V. Shvets, Thermodynamics of CeO_2 thermochemical fuel production, Energy Fuel. 29 (2) (2015) 1001–1009, https://doi.org/10.1021/ef5019912.
[28] R.J. Carrillo, J.R. Scheffe, Advances and trends in redox materials for solar thermochemical fuel production, Sol. Energy 156 (2017) 3–20, https://doi.org/10.1016/j.solener.2017.05.032.
[29] J. Lapp, J.H. Davidson, W. Lipiński, Heat transfer analysis of a solid-solid heat recuperation system for solar-driven nonstoichiometric redox cycles, J. Sol. Energy Eng. 135 (3) (2013), 031004, https://doi.org/10.1115/1.4023357.
[30] J. Lapp, W. Lipiński, Transient three-dimensional heat transfer model of a solar thermochemical reactor for H_2O and CO_2 splitting via nonstoichiometric ceria redox cycling, J. Sol. Energy Eng. 136 (3) (2014), 031006, https://doi.org/10.1115/1.4026465.
[31] R. Bala Chandran, R. Bader, W. Lipiński, Transient heat and mass transfer analysis in a porous ceria structure of a novel solar redox reactor, Int. J. Therm. Sci. 92 (2015) 138–149, https://doi.org/10.1016/j.ijthermalsci.2015.01.016.
[32] L.O. Schunk, W. Lipiński, A. Steinfeld, Heat transfer model of a solar receiver-reactor for the thermal dissociation of ZnO-Experimental validation at 10 kW and scale-up to 1 MW, Chem. Eng. J. 150 (2–3) (2009) 502–508, https://doi.org/10.1016/j.cej.2009.03.012.
[33] B. Wang, L. Li, F. Schäfer, J.J. Pottas, A. Kumar, V.M. Wheeler, W. Lipiński, Thermal reduction of iron–manganese oxide particles in a high-temperature packed-bed solar thermochemical reactor, Chem. Eng. J. 412 (May 2020), https://doi.org/10.1016/j.cej.2020.128255.
[34] V.M. Wheeler, R. Bader, P.B. Kreider, M. Hangi, S. Haussener, W. Lipiński, Modelling of solar thermochemical reaction systems, Sol. Energy 156 (2017) 149–168, https://doi.org/10.1016/j.solener.2017.07.069.
[35] B. Bulfin, Thermodynamic limits of countercurrent reactor systems, with examples in membrane reactors and the ceria redox cycle, Phys. Chem. Chem. Phys. 21 (4) (2019) 2186–2195, https://doi.org/10.1039/C8CP07077F.
[36] S. Li, V.M. Wheeler, A. Kumar, M.B. Venkataraman, C.L. Muhich, Y. Hao, W. Lipiński, Thermodynamic guiding principles for designing non-stoichiometric redox materials for solar thermochemical fuel production: ceria, perovskites, and beyond, Energy Technol. 2000925 (19) (2021) 1–18, https://doi.org/10.1002/ente.202000925.
[37] A. Lidor, T. Fend, M. Roeb, C. Sattler, Parametric investigation of a volumetric solar receiver-reactor, Sol. Energy 204 (July 2020) (2020) 256–269, https://doi.org/10.1016/j.solener.2020.04.045.
[38] S. Suter, A. Steinfeld, S. Haussener, Pore-level engineering of macroporous media for increased performance of solar-driven thermochemical fuel processing, Int. J. Heat Mass Tran. 78 (2014) 688–698, https://doi.org/10.1016/j.ijheatmasstransfer.2014.07.020.
[39] F. Cardarelli, Materials Handbook, third ed., Springer International Publishing, Cham, Switzerland, 2018 https://doi.org/10.1007/978-3-319-38925-7.
[40] E.W. Lemmon, M.O. McLinden, D.G. Friend, Thermophysical properties of fluid systems, in: P.J. Linstrom, W.G. Mallard (Eds.), NIST Chemistry WebBook, NIST Standard Reference Database Number 69, vol. 20899, National Institute of Standards and Technology, Gaithersburg MD, 2018, https://doi.org/10.18434/T4D303.
[41] I. Riess, M. Ricken, J. Nölting, On the specific heat of nonstoichiometric ceria, J. Solid State Chem. 57 (3) (1985) 314–322, https://doi.org/10.1016/0022-4596(85)90193-8.
[42] Y.S. Touloukian, D.P. DeWitt, Thermophysical Properties of Matter - the TPRC Data Series. Volume 7. Thermal Radiative Properties - Metallic Elements and Alloys, Tech. rep., Thermophysical and Electronic Properties Information Analysis Center, Lafayette, IN, Jan. 1970.
[43] O. Reutter, E. Smirnova, J. Sauerhering, S. Angel, T. Fend, R. Pitz-Paal, Characterization of air flow through sintered metal foams, J. Fluid Eng. 130 (5) (2008), 051201, https://doi.org/10.1115/1.2907419.
[44] T. Fend, B. Hoffschmidt, R. Pitz-Paal, O. Reutter, P. Rietbrock, Porous materials as open volumetric solar receivers: experimental determination of thermophysical and heat transfer properties, Energy 29 (5–6) (2004) 823–833, https://doi.org/10.1016/S0360-5442(03)00188-9.
[45] B. Bulfin, A.J. Lowe, K.A. Keogh, B.E. Murphy, O. Lübben, S.A. Krasnikov, I.V. Shvets, Analytical model of CeO_2 oxidation and reduction, J. Phys. Chem. C 117 (46) (2013) 24129–24137, https://doi.org/10.1021/jp406578z.
[46] M. Kaviany, Principles of Heat Transfer in Porous Media, 2nd Edition, Mechanical Engineering Series, Springer-Verlag, New York, 1995, https://doi.org/10.1007/978-1-4612-4254-3.
[47] S. Ackermann, M. Takacs, J. Scheffe, A. Steinfeld, Reticulated porous ceria undergoing thermochemical reduction with high-flux irradiation, Int. J. Heat Mass Tran. 107 (2017) 439–449, https://doi.org/10.1016/j.ijheatmasstransfer.2016.11.032.
[48] M. Loretz, R. Coquard, D. Baillis, E. Maire, Metallic foams: radiative properties/comparison between different models, J. Quant. Spectrosc. Radiat. Transf. 109 (1) (2008) 16–27, https://doi.org/10.1016/j.jqsrt.2007.05.007.
[49] M.F. Modest, Radiative Heat Transfer, third ed. Edition, Academic Press, New York, 2013 oCLC: ocn813855549.
[50] L.J. Venstrom, R.M. De Smith, R. Bala Chandran, D.B. Boman, P.T. Krenzke, J.H. Davidson, Applicability of an equilibrium model to predict the conversion of CO 2 to CO via the reduction and oxidation of a fixed bed of cerium dioxide, Energy Fuel. 29 (12) (2015) 8168–8177, https://doi.org/10.1021/acs.energyfuels.5b01865.
[51] K.J. Warren, J. Reim, K. Randhir, B. Greek, R. Carrillo, D.W. Hahn, J.R. Scheffe, Theoretical and experimental investigation of solar methane reforming through the nonstoichiometric ceria redox cycle, Energy Technol. 5 (11) (2017) 2138–2149, https://doi.org/10.1002/ente.201700083.
[52] S. Brendelberger, P. Holzemer-Zerhusen, H. von Storch, C. Sattler, Performance assessment of a heat recovery system for monolithic receiver-reactors, J. Sol. Energy Eng. 141 (2) (2019), 021008, https://doi.org/10.1115/1.4042241.
[53] F.P. Incropera, D.P. DeWitt, Introduction to Heat Transfer, second ed., Wiley, New York, 1990.
[54] W.M. Rohsenow, J.P. Hartnett, Y.I. Cho (Eds.), Handbook of Heat Transfer, third ed., McGraw-Hill Handbooks, McGraw-Hill, New York, 1998.
[55] L. Geissbühler, M. Kolman, G. Zanganeh, A. Haselbacher, A. Steinfeld, Analysis of industrial-scale high-temperature combined sensible/latent thermal energy storage, Appl. Therm. Eng. 101 (2016) 657–668, https://doi.org/10.1016/j.applthermaleng.2015.12.031.
[56] B. Bulfin, L. Buttsworth, A. Lidor, A. Steinfeld, High-purity nitrogen production from air by pressure swing adsorption combined with $SrFeO_3$ redox chemical looping, Chem. Eng. J. 421 (2) (2021) 127734, https://doi.org/10.1016/j.cej.2020.127734.
[57] S. Zoller, E. Koepf, P. Roos, A. Steinfeld, Heat transfer model of a 50 kW solar receiver–reactor for thermochemical redox cycling using cerium dioxide, J. Sol. Energy Eng. 141 (2) (2019), 021014, https://doi.org/10.1115/1.4042059.